



Article

# ZnO (Ag-N) Nanorods Films Optimized for Photocatalytic Water Purification

Luis Sanchez <sup>1</sup>, Carlos Castillo <sup>1</sup>, Willy Cruz <sup>1</sup>, Bryan Yauri <sup>1</sup>, Miguel Sosa <sup>1</sup>, Clemente Luyo <sup>1</sup>, Roberto Candal <sup>2,3</sup>, Silvia Ponce <sup>4</sup> and Juan M. Rodriguez <sup>1,\*</sup>

<sup>1</sup> Center for the Development of Advanced Materials and Nanotechnology, Universidad Nacional de Ingeniería, Av. Tupac Amaru 210, Rimac, Lima 15333, Peru; lasr\_uni@hotmail.com (L.S.); castillocorreac@gmail.com (C.C.); cruzbw@outlook.es (W.C.); bryan.yauri@hotmail.com (B.Y.); miguel7101992@gmail.com (M.S.); clemente\_luyo@yahoo.com (C.L.)

<sup>2</sup> Escuela de Ciencia y Tecnología, Universidad Nacional de San Martín, San Martín 1650, Argentina; rjcandal@gmail.com

<sup>3</sup> Instituto de Investigación e Ingeniería Ambiental, CONICET, Universidad Nacional de San Martín, San Martín 1650, Argentina

<sup>4</sup> Facultad de Ingeniería Industrial, Universidad de Lima, Av. Javier Prado Este 4600, Santiago de Surco, Lima 15023, Peru; spponceal@gmail.com

\* Correspondence: jrodriguez@uni.edu.pe

Received: 24 July 2019; Accepted: 4 November 2019; Published: 19 November 2019



**Abstract:** ZnO nanorods (NRs) films, nitrogen-doped (ZnO:N), and ZnO doped with nitrogen and decorated with silver nanostructures (ZnO:N-Ag) NRs films were vertically supported on undoped and N doped ZnO seed layers by a wet chemical method. The obtained films were characterized structurally by X-ray diffraction. Morphological and elemental analysis was performed by scanning electron microscopy, including an energy dispersive X-ray spectroscopy facility and their optical properties by Ultraviolet-Visible Spectroscopy. Analysis performed in the NRs films showed that the nitrogen content in the seed layer strongly affected their structure and morphology. The mean diameter of ZnO NRs ranged from 70 to 190 nm. As the nitrogen content in the seed layer increased, the mean diameter of ZnO:N NRs increased from 132 to 250 nm and the diameter dispersion decreased. This diameter increase occurs simultaneously with the incorporation of nitrogen into the ZnO crystal lattice and the increase in the volume of the unit cell, calculated using the X-ray diffraction patterns and confirmed by a slight shift in the XRD angle. The diffractograms indicated that the NRs have a hexagonal wurtzite structure, with preferential growth direction along the *c* axis. The SEM images confirmed the presence of metallic silver in the form of nanoparticles dispersed on the NRs films. Finally, the degradation of methyl orange (MO) in an aqueous solution was studied by UV-vis irradiation of NRs films contained in the bulk of aqueous MO solutions. We found a significant enhancement of the photocatalytic degradation efficiency, with ZnO:N-Ag NRs film being more efficient than ZnO:N NRs film, and the latter better than the ZnO NRs film.

**Keywords:** spray pyrolysis; ZnO; nanorods; nitrogen-doped; photocatalysis

## 1. Introduction

The use of nanostructured semiconductors for photocatalysis has attracted significant attention due to their potential applications for water and air decontamination [1–3]. Among the various semiconductor photocatalysts, titanium dioxide (TiO<sub>2</sub>) in its anatase crystalline form and zinc oxide (ZnO) in its wurtzite crystalline form are the most promising (see for example [4] and references therein). Favorable position of the bands energy of ZnO with respect to TiO<sub>2</sub> expects a more efficient photocatalytic performance [4,5]. The 3.37 eV of its optical bandgap at room temperature, the 60 eV

of exciton energy [6], added to the fact that it is a GRAS (Generally Recognized as Safe) material and present a large variety of morphologies allows ZnO to be considered a promising candidate for photocatalytic water purification [7–10]. 1D structures [11–14] presents a charge transport property different from those of spheroidal nanoparticles, modifying positively its surface-to-volume ratio and electrochemical double layer, resulting in an enhancement of the photocatalytic efficiency [15]. However, its wide bandgap and the electron-hole recombination are two of the main drawbacks of the ZnO nanostructures. Therefore, considerable efforts are being dedicated to overcome these problems, particularly by extending its absorption to the visible part of the solar spectrum and by reducing electro-hole recombination [16,17]. Using nonmetals as a carbon, nitrogen, and sulfur results in a modification of the conduction band to more negative potentials, then narrowing the optical bandgap, i.e. enlarging the absorption to lower energies of the solar spectra [18–21]. In the case of nitrogen, a slight shift to the blue [22] and red [23] were reported in the literature. The blue shift was associated to the presence of defects on the structure of the doped ZnO. Photocatalytic efficiency of ZnO NRs can be further increased by the formation of heterostructured photocatalysts by associating ZnO and noble metal particles. This effect is due to the well-known electron collector capacity of metal nanoparticles, that improve charge carriers separation decreasing, thus, the recombination [24,25]. For instance, it has recently been reported that ZnO doped with silver nanoparticles improves the electron transfer process and photochemical stability, making them a better photocatalyst [26–28].

The incorporation of different dopants leads to the modification of the synthesis conditions, and consequently, it may lead to the modification of the microstructure and/or morphology of ZnO particles. This phenomenon is considerably less explored in the literature than the effect of doping on electronic structure, but it also affects the performance of the photocatalyst. As far as we know, there are no previous reports about the effects of nitrogen content in the seed layers on the properties of the nanorods grown from these seeds and deposited by spray pyrolysis technique (SPT). SPT is a low cost, easy-to-use, safe, simple, and reproducible way to control the seeds deposition [29]. The aim of this work is to present the synthesis by wet chemistry of ZnO NRs, nitrogen-doped (ZnO:N) NRs, and silver-decorated nitrogen-doped (ZnO:N-Ag) NRs on a transparent and electrically conductive glass substrate. The emphasis is focus on the relationship between morphology, structure, optical, and photocatalytic properties of the obtained supported NRs with the nitrogen content in the seed layers.

## 2. Experimental and Methods

### 2.1. Materials

We used analytical grade zinc acetate [ $\text{Zn}(\text{CH}_3\text{COO})_2 \cdot 6\text{H}_2\text{O}$ , Merck, Darmstadt, Germany] and ammonium acetate [ $\text{CH}_3\text{COONH}_4$ , Merck, Darmstadt, Germany] as precursors of ZnO and ZnO:N, respectively. Zinc nitrate [ $\text{Zn}(\text{NO}_3)_2 \cdot 6\text{H}_2\text{O}$ , Sigma-Aldrich, Steinheim, Germany] and hexamethylenetetramine (HMT), [ $\text{C}_6\text{H}_{12}\text{N}_4$ , Merck, Darmstadt, Germany] were used to prepare the NRs growth solutions. All reagents were used as received.

A transparent and electrically conductive  $\text{SnO}_2:\text{F}$  film of  $8 \Omega/\text{sq}$  of sheet resistance (FTO) was used as a substrate for the growth of undoped ZnO and ZnO:N NRs following a cleaning process [29]. In brief,  $2.0 \times 1.5 \text{ cm}^2$  pieces of FTO conductive glass were cleaned in an ultrasonic bath, first with water and then with ethanol, before depositing the seed layer.

### 2.2. Seed Deposition

Undoped ZnO and ZnO:N seeds layers were deposited onto FTO substrates using SPT [29]. The seed layers were then used as a substrate to allow us to obtain undoped ZnO and ZnO:N NRs. In total, five precursor solutions were prepared to obtain pure and doped seed layers. To obtain a pure ZnO seed layer, a 0.5 mol/L solution of zinc acetate in water was used. ZnO:N seed layers with an increasing amount of nitrogen were obtained by using four different precursor solutions. These were prepared by mixing solutions of 0.5 mol/L of zinc acetate and 2.5 mol/L of ammonium acetate in water

with different volume ratios ( $\Gamma$ ), keeping constant the volume of the zinc acetate solution and adding different volumes of ammonium acetate solution. In total, four ZnO:N seed layers were prepared ( $\Gamma = 1:1, 1:2, 1:3, 1:4$ ). In order to ensure total dissolution as well as to adjust the pH to 5.5, a few drops of  $\text{CH}_3\text{COOH}$  were added to the five prepared solutions. The pure ZnO seed layer and the ZnO:N seed layers prepared with the four different volume ratios mentioned previously are hereafter referred to as ZnO, ZnO:N (1:1), ZnO:N (1:2), ZnO:N (1:3), and ZnO:N (1:4), respectively. Finally, a homemade spray pyrolysis system was used to deposit the seed layers as it was described in detail elsewhere [30]. In brief, a medical nebulizer was used as atomizer to produce uniform size droplets which were directed by a nozzle towards the hot substrate at 350 °C, keeping constant the 5 mm distance from the nozzle to the substrate. The hot substrate performed an oscillating movement at constant velocity to cover the whole area of the substrate. Micro-filtered air was used as a carrier gas at a fixed pressure of  $1.7 \times 10^5$  Pa and maintained at a constant flux of 10 L/min.

### 2.3. The Growth of ZnO and ZnO:N NRs Films

In order to grow ZnO and ZnO:N NRs films from the ZnO and ZnO:N seed layer respectively, a simple hydrothermal process was used and two solution growth were prepared. The first solution, used to grow undoped ZnO NRs from undoped ZnO seed layer, was prepared by mixing equal volumes of  $\text{C}_6\text{H}_{12}\text{N}_4$  (0.1 M) and  $\text{Zn}(\text{NO}_3)_2 \cdot 6\text{H}_2\text{O}$  (0.1 M) in water. The second solution used to grow ZnO:N NRs from the ZnO:N seed layers was prepared by mixing equal volumes of the following solution:  $\text{Zn}(\text{NO}_3)_2 \cdot 6\text{H}_2\text{O}$  (0.1 M),  $\text{C}_6\text{H}_{12}\text{N}_4$  (0.1 M), and  $\text{CH}_3\text{COONH}_4$  (0.1 M) in water. Then, a substrate containing the seed layers of ZnO or ZnO:N were placed in a 100 mL screw-capped glass flasks containing 40 mL of the solution growth. This glass flask containing the substrate and the solution growth was placed in an oven at 90 °C for 1 h. After that, the substrate, covered with ZnO or ZnO:N NRs was then obtained, removed from the glass flask, and gently cleaned with distilled water and ethanol. Finally, the substrates with NRs film were dried at room temperature.

### 2.4. Photodeposition of Silver

In order to ensure the surface modification of undoped ZnO and ZnO:N NRs with silver nanostructures, 10 mL of a 10 mM solution of  $\text{AgNO}_3$  (99% in purity from Sigma-Aldrich, Saint Louis, MO, USA) in water was prepared. Then, the as fabricated ZnO and ZnO:N NRs films were submerged in the  $\text{AgNO}_3$  solution and exposed for 20 min to 1.9 mW/cm<sup>2</sup> of UV light in order to obtain photo reduction. An Ultra Vitalux 300 W OSRAM lamp was used as a source of light. After the treatment, the final product was washed with ethanol and distilled water and then dried at 60 °C.

### 2.5. Photocatalytic Characterization

Undoped ZnO, ZnO:N, and ZnO:N-Ag NRs films ( $2.5 \times 1.5$  cm<sup>2</sup>) were placed at the bottom of a vessel with the NRs pointing upward to test the photocatalytic degradation of 50 mL methyl orange (MO) water solution under a constant stirring. The reactor system used to study the photocatalytic decomposition of MO is shown in Figure S1a. The light source Ultra Vitalux 300 W OSRAM lamp (OSRAM, Wilmington, USA) in Figure S1b shows its emission spectra determined with an Oceanoptics USB 4000 spectrometer, (Oceanoptics, Largo, FL, USA) was placed approximately 25 cm above the sample, for which 6.5 mW/cm<sup>2</sup> in the UV-A range of intensity was measured. The initial concentration of MO was 3 mg/L. Experiments were performed in a natural environment without controlling the temperature ( $22 \text{ }^\circ\text{C} \pm 2 \text{ }^\circ\text{C}$ ). 2.5 mL of the treated solution was collected each hour in order to analyze with an UV-Vis spectrophotometer the MO concentration.

### 2.6. Characterization Methods

The micromorphology of NRs films was studied using a scanning electron microscopy HITACHI SU8230 (Hitachi, Omuta, Japan). ImageJ 1.52r software was used in order to obtain the nanorod statistics. The elemental composition was determined by EDS. The crystalline structure of the NRs

was determined by X-ray diffraction using a Philips X'PERT MPD (Malvern Panalytical, Malvern, United Kingdom) with Cu-K $\alpha$  radiation equipment. The transmittance of each film was measured with a spectrophotometer Lambda 25 Perkin Elmer (PerkinElmer, Waltham, USA) working in the range within 190 nm to 1100 nm

### 3. Results and Discussion

Figure 1a–d show SEM images of ZnO:N(1:0), ZnO:N(1:1), ZnO:N(1:2), and ZnO:N(1:4) NRs films, respectively. All NRs exhibited hexagonal cross sections and generally grew perpendicular to the surface. The diameter, density, and the thickness of the NR films displayed a clear trend with the amount of N at the solution used to prepare the seed layers. The micrographs show that ZnO NRs grown onto an undoped seed layer were thinner, more dispersed, and worse oriented than ZnO:N NRs grown onto N-doped ZnO seed layers. When the N content in the seed layer increases, the diameter and the film thickness of ZnO:N NRs films increases, while the dispersion in NRs diameter sizes slightly decreased. The thickness of the ZnO NRs films increased continuously from 1.3  $\mu\text{m}$  to 2.4  $\mu\text{m}$  when the nitrogen content in the ZnO:N increased from (1:0) to (1:4), respectively. The mean nanorod diameter increased from 128 nm to 250 nm for ZnO NRs grown on undoped ZnO seed layers with respect to the ZnO:N NRs grown on N-doped ZnO seed layer, respectively. The right side of Figure 1 shows the NRs frequency of diameters in the ZnO:N NRs films. The mean diameter and size dispersion of NRs are shown in Figure 2a and also reported in Table 1 for all the samples. Figure 2b shows the average number of rods counted on  $5 \times 5 \mu\text{m}^2$  squares located at different positions at the surface of the samples. The number of NRs decreased as the N concentration increased in the seed layer. From the mean diameter ( $2R$ ), the NRs counted ( $N$ ) on flat areas and the film thickness ( $d$ ), we can estimate the surface area  $A_S$  of NRs considering a rod as a hexagonal prism using the following relation:

$$A_S = \left( \frac{3}{2} R^2 \sqrt{3} + 6R * d \right) * N. \quad (1)$$

Figure 2b shows the values of  $A_S$ , the calculated surface area of NRs, for the  $5 \times 5 \text{ mm}^2$  squares of analyzed surface as mentioned previously. Clearly, the NR surface area increased with the increase of N concentration in the seed layer. The NRs that grew from the ZnO:N (1:4) seed layer had the largest surface area.

The increase in the mean diameter, shown in Figure 2a, can be attributed to the increase in particles size in the seed layer [31–33]. Nitrogen dopant introduced in the ZnO seed layer increase the particle size of seed layer, and as each particle acts as a nucleation site for the growth of the nanorods, it results in the growth of nanorods with bigger diameters. Moreover, when the particle size of seed layer increases the density of nucleation site decrease and therefore the number of nanorods per unit of surface area decreases, this is in good agreement with results shows in Figure 2b. The less density of nanorods with bigger diameter and better alignment, as show in Figure 1, promoted rapid growth along the vertical direction result in films of bigger thickness [34,35].

The elemental composition of the ZnO NRs and ZnO doped with nitrogen NRs were obtained by EDS spectroscopy. A typical EDS spectrum of undoped ZnO NRs is shown in Figure S4a. Signals corresponding to the presence of Zn, O, C, and Sn can be clearly identified. The C and Sn peaks came from the FTO substrate. No any other element was detected. In Figure S4b, the EDS spectra of the ZnO:N (1:3) NRs film is presented. As can be seen from the inset, a weak peak at 0.39 eV corresponding to nitrogen is observed. This provides direct evidence that nitrogen atoms were introduced into the ZnO NRs film. The N content in the film was estimated at about 0.9 at.%. However, with this technique, nitrogen was detected only in this film.

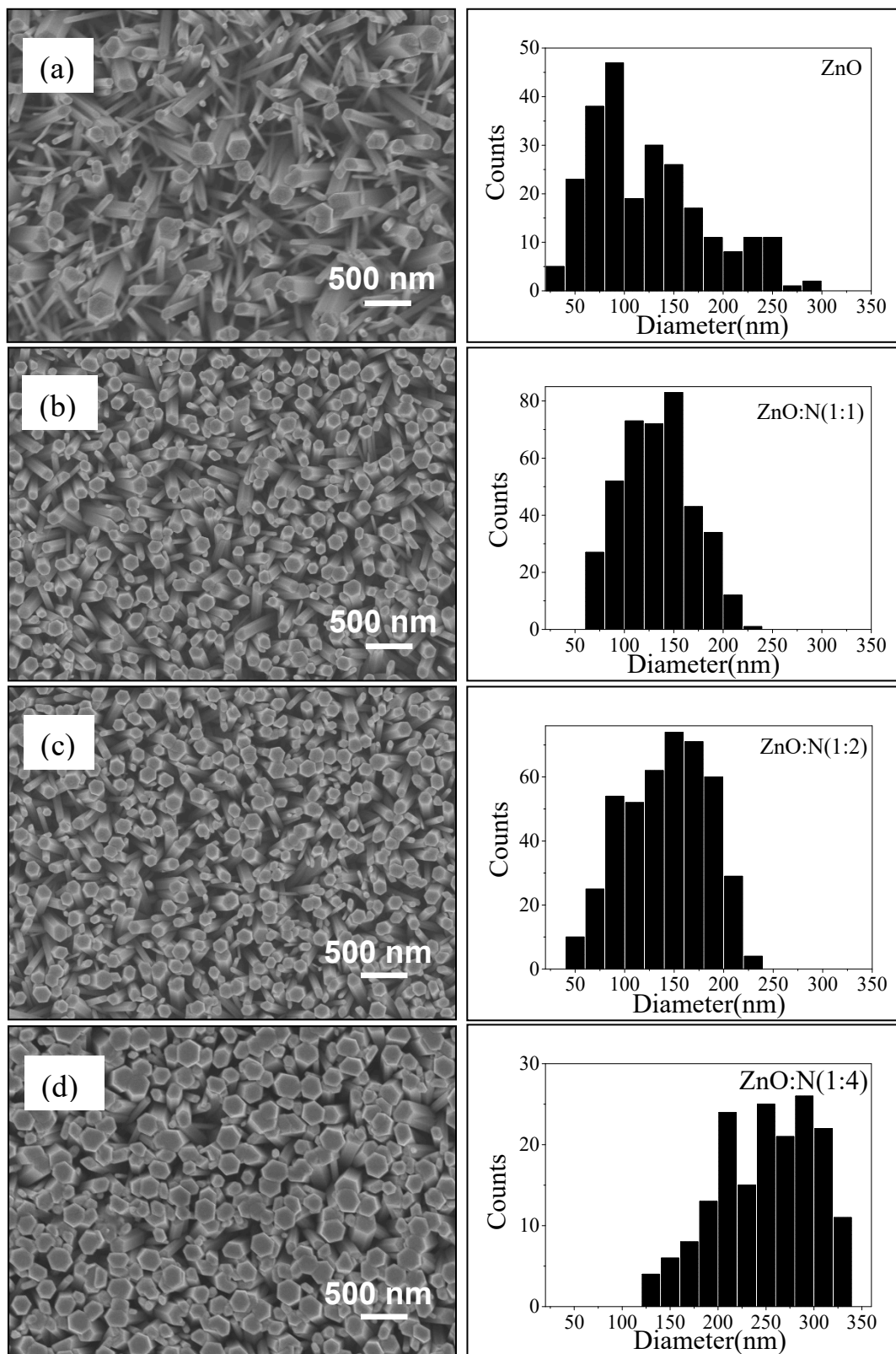


**Figure 1.** Left: electronic micrographs of (a) ZnO (1:0), (b) ZnO:N (1:1), (c) ZnO:N (1:2), and (d) ZnO:N (1:4); right: the corresponding NRs diameter distribution obtained through the software ImageJ.

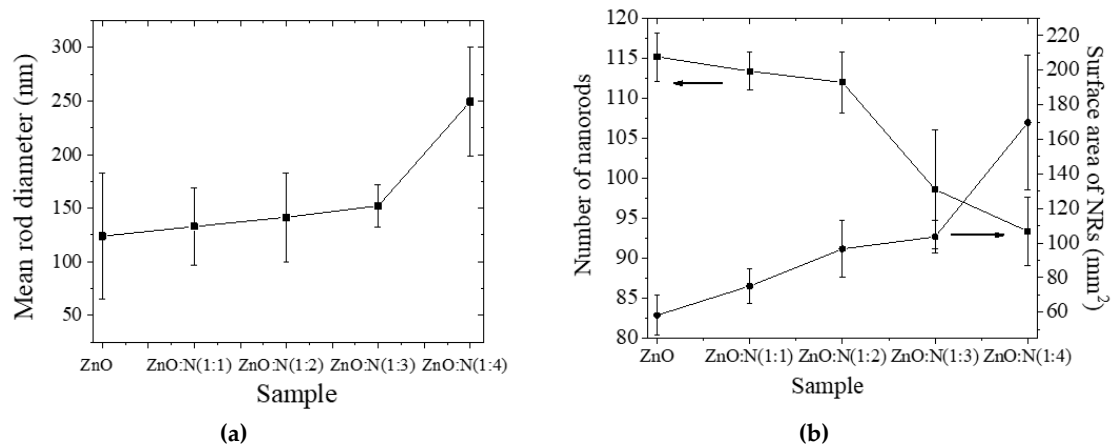


**Figure 2.** (a) Mean diameter and dispersion of the ZnO NRs; (b) Surface area calculated by equation (1) and number of NRs counted on different  $5 \times 5 \mu\text{m}^2$  squares at the sample surface.

**Table 1.** Summary of results: (a) thickness of the films (estimated from cross-sectional SEM images shown in Figure S2); (b) mean NR diameter (obtained from SEM images); (c) optical transmittance at 550 nm; and (d) Onset of absorption edge as extracted from the extrapolation of the linear part of the absorption spectra (for further details see Figures S2 and S3, and Appendix A).

Sample	Film Thickness from Micrographs $d$ (nm)	Mean Diameter of the Nanorods from Micrographs (nm)	Optical Transmittance, 550 nm (%)	Onset of Absorption Edge (eV)
Bare FTO	$346 \pm 5$	-	82	-
ZnO Pure	$1290 \pm 180$	$128 \pm 58$	2.7	3.27
ZnO:N (1:1)	$1645 \pm 108$	$132 \pm 35$	8.9	3.25
ZnO:N (1:2)	$2010 \pm 100$	$141 \pm 41$	10.5	3.26
ZnO:N (1:3)	$2272 \pm 107$	$152 \pm 19$	9	3.27
ZnO:N (1:4)	$2380 \pm 78$	$249 \pm 50$	13.8	3.27

Figure 3a,b shows typical scanning electron images of as-synthesized pure ZnO and ZnO:N (1:2) NRs after the Ag photodeposition process, respectively. The presence of nanoparticles on the ZnO:N (1:2) NRs is clearly noticeable in Figure 3b. Figure S5 shows an SEM images obtained with an energy selective backscattered electron detector (ESB) of sample ZnO:N (1:2) in the same position of as show in Figure 3b, the color contrast difference on ESB analysis clearly indicates that the elemental composition of nanoparticles differ from the ZnO rods. Figure 3c depicts the EDS spectrum corresponding to the region of the film shown in Figure 3a (ZnO-Ag NRs), indicating that silver is present in this system. EDS and ESB analysis confirm that nanoparticles are indeed silver nanoparticles. Silver was deposited in the form of nanoparticles on the top and lateral faces of the ZnO:N rods, but in the case of the pure ZnO rods, although it is detected by EDS, cannot be identified as well-defined particles. To determine the reason of this behavior a deeper study of this phenomenon is necessary. Very likely, it is consequence of the presence of a higher amount of thick rods in the ZnO:N samples.



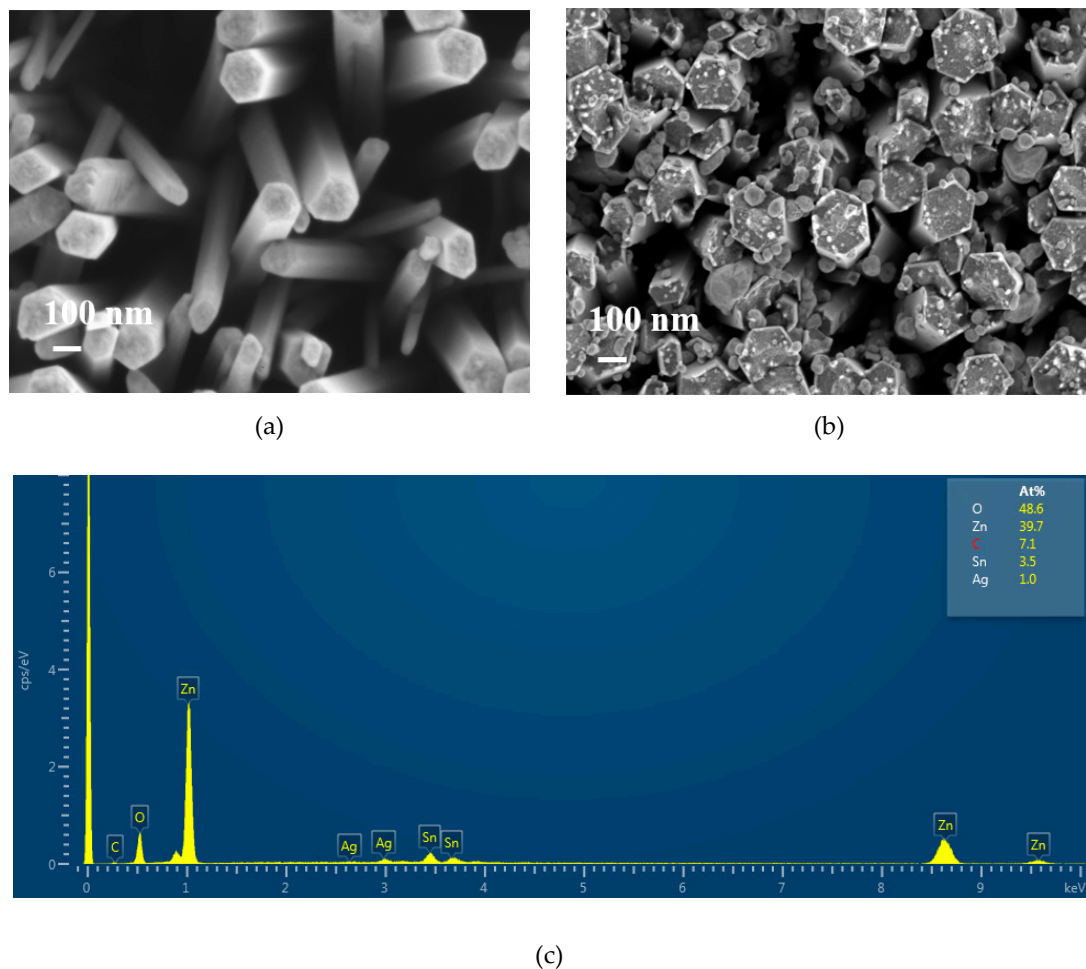


**Figure 3.** SEM analysis of (a) ZnO-Ag, (b) ZnO:N-Ag NRs, and (c) Elemental EDS spectrum of ZnO-Ag sample.

Figure 4a presents the X-ray diffraction patterns of ZnO and ZnO:N films of nanorods grown on seeds with different ZnO:N ratios. All the samples displayed high crystallinity with an average crystalline grain size between 44 and 51 nm, depending on seed composition. The main peaks of the diffractograms can be attributed to the hexagonal structure of ZnO wurtzite corresponding to the crystalline planes (100), (002), (101), (102), (103), and (112) [JCPDS card No. 36-1451]. The most intense diffraction plane is (002) and indicates that the *c*-axis of the wurtzite structure is the preferred growth direction for the supported nanorods. Meanwhile, the weak diffraction peaks corresponding to the crystalline planes (100) and (101) tend to disappear as the nitrogen content in the seed layer increases. Peaks marked with (\*) are peaks corresponding to the transparent conductive substrate, with no additional diffraction peak detected. Figure 4b shows an amplified view of the reflection corresponding to the crystalline plane (002) of undoped and nitrogen-doped ZnO nano-films. It can be clearly observed that the presence of nitrogen slightly shifts the position of the diffraction peak towards a smaller diffraction angle. This would prove a successful doping due to a possible substitutional modification of the oxygen, or in any case, interstitial, since the nitrogen atom is larger than the oxygen atom but smaller than the zinc atom, thus increasing the lattice constant [36]. Figure 4c shows the ratio of the relative intensity for the (101) and the (002) peaks corresponding to the different NRs films. The decreasing trend indicates that the *c*-axis alignment improved as the N content of the seed layer increased.

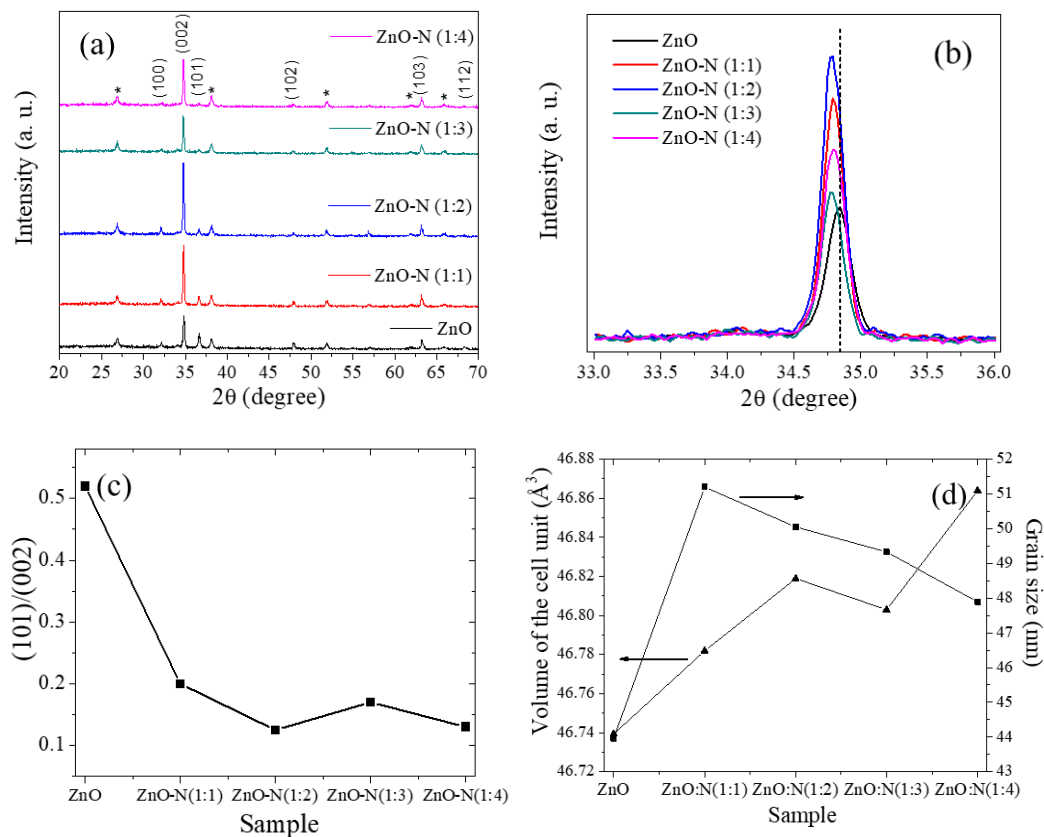


**Figure 4.** The ZnO and ZnO:N NRs films shown: (a) the diffraction patterns, (b) an enlarged view of the diffraction peak associated to the crystalline plane (002), (c) relative intensity ratio of (101)/(002) peaks, and (d) volume of the unit cell and grain size.

Applying the Debye-Scherrer equation,  $D = 0.9\lambda/\beta\cos\theta$ , [37] to the crystalline plane (002) allow us to calculate the crystalline grain size along the c-axis. In this equation,  $\beta$  is the full width at half maximum of the peaks corresponding to the crystalline plane (002),  $\lambda = 1.540598 \text{ \AA}$  and  $\theta$  the diffraction angle. The calculated  $D$  for all samples is shown in Figure 4d. In general, the grain size for all ZnO:N NRs is larger than for undoped ZnO, with the grain size of ZnO:N (1:1) being the largest. Figure 4d also shows that for ZnO:N NRs, the grain size decreases as the N content in the seed layer increases.

The lattice parameters 'a' and 'c' were calculated by using the relation of  $r$  spacing [37]

$$\left(\frac{1}{r_{hkl}}\right)^2 = \frac{4}{3}\left(\frac{h^2 + k^2 + hk^2}{a^2}\right) + \frac{l^2}{c^2}. \quad (2)$$

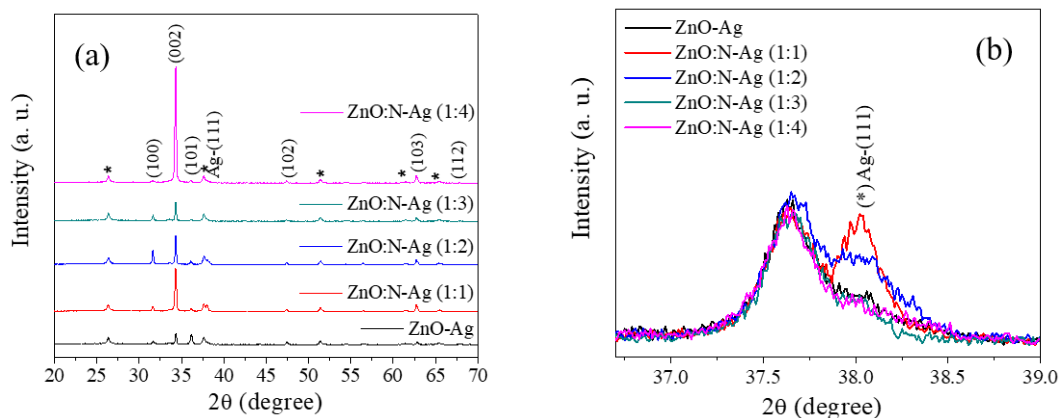
The lattice parameters and the  $c/a$  ratios are shown on Table 2, as well as the unit cell volume, which is also plotted on Figure 4d. The calculated  $c/a$  ratio of about 1.603 which is correlated with the 1.633 published elsewhere [23]. All ZnO:N samples exhibit bigger crystal parameters as compared to pure ZnO.

**Table 2.** Calculated lattice parameter for pure ZnO, ZnO:N, and ZnO:N-Ag (1:1) NRs films.

Sample	FWHM (°)	$2\theta$ (°)	Grain Size D (nm)	Crystal Parameters			Volume ( $\text{\AA}^3$ )
				a = b ( $\text{\AA}$ )	c ( $\text{\AA}$ )	c/a	
ZnO	0.220	34.84	44.0	3.2290	5.1763	1.603	46.739
ZnO:N (1:1)	0.189	34.79	51.0	3.2293	5.1799	1.604	46.782
ZnO:N (1:2)	0.193	34.78	50.0	3.2305	5.1801	1.603	46.819
ZnO:N (1:3)	0.196	34.77	49.0	3.2302	5.1795	1.603	46.803
ZnO:N (1:4)	0.202	34.79	48.0	3.2329	5.1776	1.602	46.864
ZnO:N-Ag (1:1)	0.335	38.05	30.0	-	-	-	-

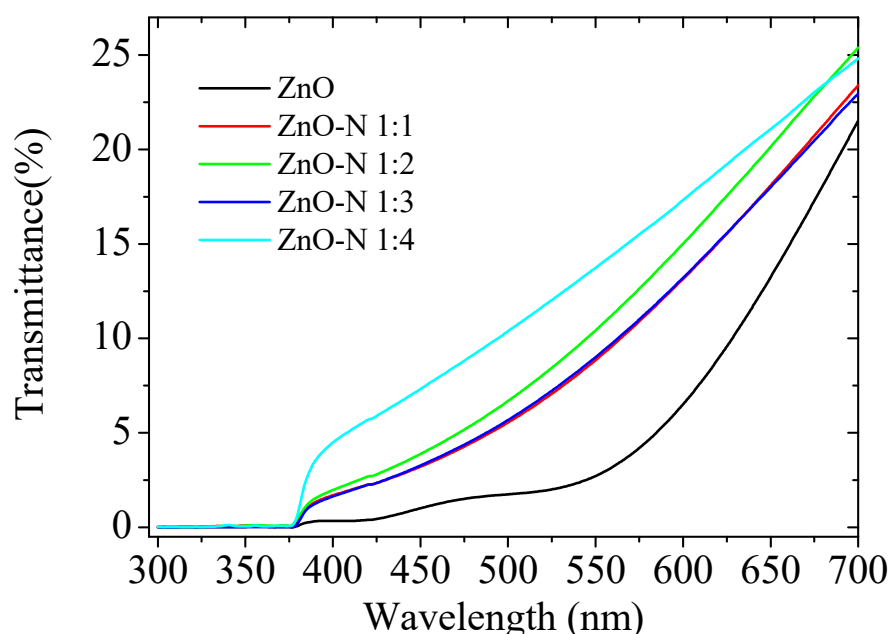


Figure 5a presents the diffractograms of the ZnO and ZnO:N NRs films after the photoreduction process. There is no obvious difference with the XRD patterns shown in Figure 4a, as both graphs display the same peaks. However, an enlarged view of the FTO peak at  $37.65^\circ$ , shown in Figure 5b, reveal the presence at  $38.05^\circ$  of one weak peak (\*). The presence of this diffraction peak can be assigned to the plane (111) of the FCC Ag structure [JCPDS card no. 04-0783], associated with crystalline nanostructures of Ag in films. In addition, the fact that there are no additional diffraction peaks associated to this element is probably due to the fact that they are only attached on the NRs surface. The calculated grain size corresponding to the peak (111) of the Ag nanoparticles was 30 nm.



**Figure 5.** (a) XRD patterns of Ag-decorated undoped and ZnO:N NRs with different nitrogen contents in the seed layer; (b) enlarged view of the FTO peak shown in Figure 5a.

The optical transmittance spectra of the ZnO and ZnO:N NRs films were recorded over the spectral range of 300–700 nm and are shown in Figure 6. In general, the transmittance was below 15% (at  $\lambda = 550$  nm) for all samples and the lowest transmittance was for undoped ZnO, the results of this analysis for the different samples are summarized in Table 1. The onset of the absorption edge (see Table 1, the supplementary material and references [38,39] for further details). The average transmittance increased with doping, likely due to an increase in the axial order of the synthesized ZnO:N NRs.



**Figure 6.** Spectral transmittance in the visible range of ZnO and ZnO:N NRs films.

The absorption onsets are similar for all synthesized materials, only a small reduction in the onset of absorption was found for all the ZnO:N films as compared to pure ZnO. This reduction may be due to substitution of N for O and later formation of Zn–N bonds. The existence of Zn–N bonds can result in mixing of N  $2p$  states and O  $2p$  states, which can account for the restructuring of the valence band and subsequent reduction of band gap [40]. However, no significant changes in the absorption onsets are similar for ZnO and ZnO:N materials

The photocatalytic activity of all the samples is shown in Figure 7.  $C_0$  represents the initial concentration of MO and  $C$  is the MO concentration after light exposure. As a reference on both graphs, the green line shows the degradation of MO under direct light illumination in absence of photocatalyst; almost no degradation was observed.

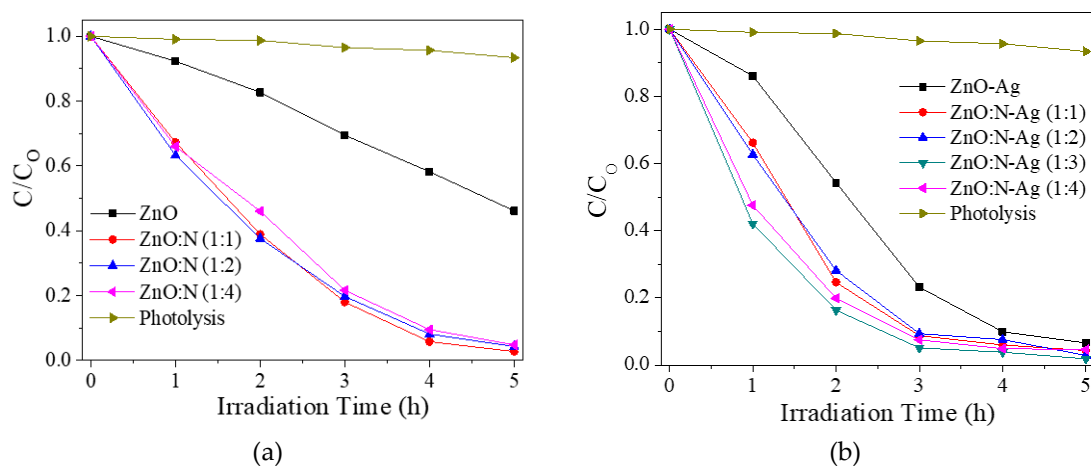


**Figure 7.** Variation of the photocatalytic efficiency of (a) pure ZnO and ZnO:N NRs and (b) ZnO-Ag and ZnO:N-Ag NRs. Uncertainty associated with each measurement is 5%.

Figure 7a shows the photocatalytic activity of pure ZnO and ZnO:N NRs. An important enhancement of photocatalytic activity is observed. All ZnO:N NRs photocatalysts exhibited a higher degradation rate than pure ZnO NRs, with ZnO:N (1:1) being slightly the most efficient by removing 98% of the dye in 5 h. By contrast, during the same amount of time, only 55% of the dye was degraded by using pure ZnO NRs. No big differences were found in the degradation rate between all ZnO:N NRs films. The higher photocatalytic performance of ZnO:N NRs as compared to pure ZnO NRs films is likely due mainly to their bigger surface area and crystal size than pure ZnO NRs, as can be clearly seen in Figure 2 and Table 2 respectively, and to a lesser extent, to a small enhanced of visible light absorption capacity due to nitrogen doping. As explained in [41], nitrogen dope introduces surface states due to defects, reducing then optical bandgap [42] by adding a band tail.

The photocatalytic activity of ZnO-Ag and ZnO:N-Ag NRs films are displayed in Figure 7b. There is a significant enhancement of photocatalytic activity due to the presence of silver in these materials with respect to pure ZnO and ZnO:N NRs (shown in Figure 8a). All ZnO:N-Ag NRs films degrade around 95% of the MO in only three h.

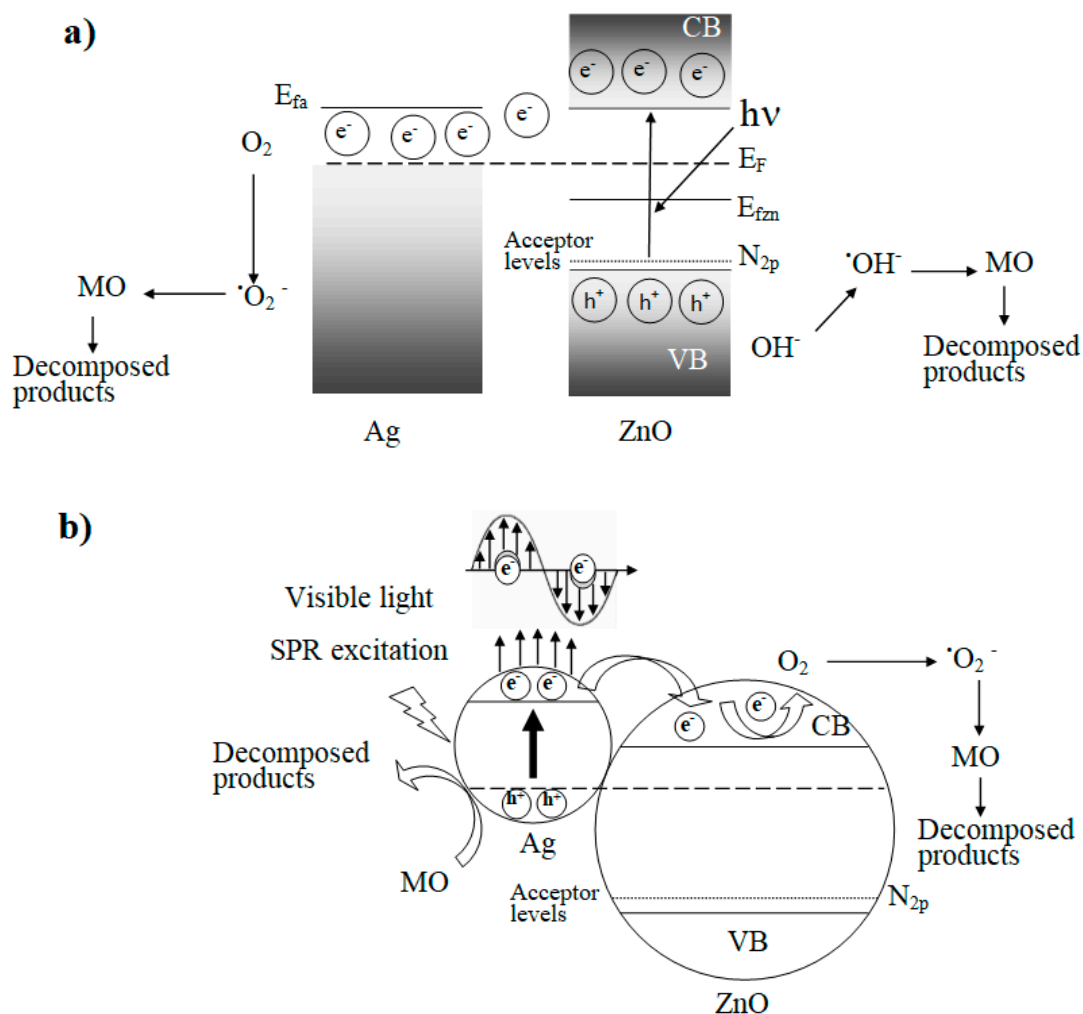


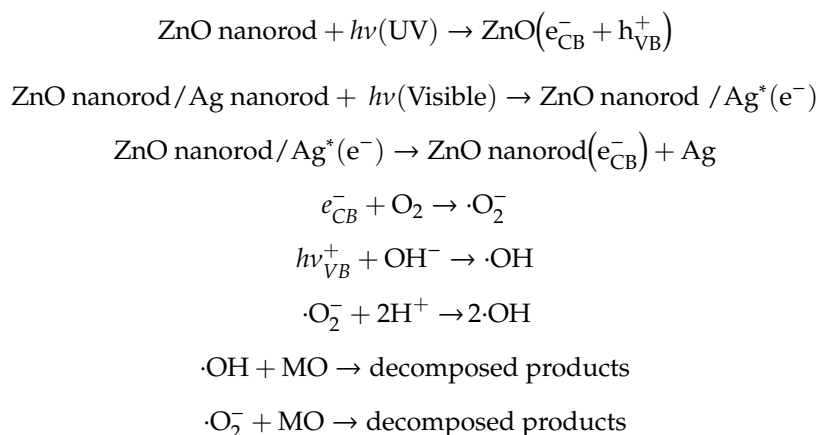
**Figure 8.** Schematic band diagram of ZnO:N-Ag nanostructures showing the processes for the photocatalytic degradation of MO dye under (a) UV light irradiation and (b) visible light irradiation.

The energetic position of the energy bands to ensure rapid transfer of photo-induced charge carriers in nitrogen doped and silver-decorated ZnO films has been discussed before [22,23,26–28]. Figure 8 shows a scheme that resumes the different processes that takes place during the photocatalytic degradation of MO under UV or visible light illumination. The influence of silver on a semiconductor promotes the formation of a Schottky barrier, behaving as a container for these, which improves the separation of photogenerated charge carriers. This allows electrons to flow from the ZnO to the Ag nanostructures, since the lower energy level of the ZnO conduction band is higher than the Fermi equilibrium energy level ( $E_f$ ) of the ZnO-Ag heterostructures. On the other hand, the positive charge carriers can, in principle, remain on the semiconductor surfaces, as shown in Figure 8a. Then, each of the charge carriers will follow the well-known adsorption processes and redox reactions, producing superoxides  $\bullet\text{O}_2^-$  in the conduction band and hydroxyl radicals  $\bullet\text{OH}$  on the valence band. This will lead to methyl orange until it is broken down into  $\text{CO}_2$  and  $\text{H}_2\text{O}$ .

On the other hand, the increase of photoactivity in the visible range can be rationalized with the mechanism described in Figure 8b. Where plasmon resonance under visible radiation produces on the silver nanostructures a promotion of charge carriers [43–46], adding the fact that the Schottky interfacial barrier would prevent the transfer of an electron from the surface of the silver nanostructure to the semiconductor. However, it has been shown that electrons are still able to be transferred back from the Ag to the ZnO:N due to the strong collective oscillation of electrons under the plasmon

excitation [47–49]. As in the previous case, the photogenerated superoxide  $\bullet\text{O}_2^-$  and hydroxyl  $\bullet\text{OH}$  radicals would be generated and react with the MO.

The overall reactions under the UV and Visible photocatalytic reaction are shown below [45]:



#### 4. Conclusions

ZnO, nitrogen-doped ZnO (ZnO:N) and silver-decorated nitrogen-doped ZnO (ZnO:N-Ag) nanorods (NRs) films were grown vertically on undoped and N doped ZnO seed layers by a wet chemical method. The diameter, density of the NRs, and the thickness of the NR films were strongly influenced by the properties of seed layers. The SEM analysis shows that ZnO NRs grown on undoped seed layer were thinner, more dispersed and worse oriented than ZnO:N NRs grown on N-doped ZnO seed layers. When increasing N content in the seed layer, the diameter of ZnO:N NRs, surface area, and the thickness of the films also increase, but the spread of diameter sizes decrease. Ag was photodeposited as nanoparticles attached on the surface of the ZnO:N nanorods, but was amorphously and dispersed on the ZnO NRs. This different behavior might be associated with size NRs. A significant enhancement of the photocatalytic efficiency of ZnO:N NRs as compared with pure NRs was determined. Besides, the subsequent decoration of the ZnO:N NRs with Ag hetero-structures resulted in an additional enhancement of the photocatalytic efficiency, with ZnO:N-Ag generally being more efficient than ZnO:N and the latter better than pure ZnO nanorods.

**Supplementary Materials:** The following are available online at <http://www.mdpi.com/2079-6412/9/11/767/s1>, Figure S1: (a) Photocatalytic reactor system and (b) emission spectra of the 300 W OSRAM Ultravitalux lamp, Figure S2: SEM images of the cross section NRs films prepared under different conditions of seed deposition: (a) ZnO, (b) ZnO:N (1:1), (c) ZnO:N (1:3) and (d) ZnO:N (1:4), Figure S3:  $(\alpha \cdot h\nu)^2$  vs.  $h\nu$  plots derived from transmittance spectra for ZnO for undoped ZnO and ZnO:N NRs films. Inset shows the extrapolation exclusively for the ZnO:N NRs films, Figure S4: Typical elemental analysis spectrums of ZnO NRs films (a) and ZnO:N NRs films (b), Figure S5: Backscattered electron micrograph of sample ZnO:N (1:2).

**Author Contributions:** Conceptualization, J.M.R. and R.C.; methodology, C.C.; validation, B.Y.; formal analysis, L.S.; investigation, S.P., C.C., W.C., B.Y. and M.S.; resources, S.P., C.L.; writing—original draft preparation, L.S.; writing—review and editing, R.C.; visualization, C.L.; supervision, J.M.R.; project administration, L.S.; funding acquisition, L.S.

**Funding:** This research was funded by Peruvian National Fund for Scientific, Technological Development and Technological Innovation (FONDECYT), grant number 120-2018-FONDECYT

**Acknowledgments:** This work was supported by the Projects N° 223-2015-FONDECYT, 120-2018-FONDECYT, N° 113-INNOVATE PERU-ISASS-2018, and by PICT 2016-2386, ANPCyT, Argentina); The Authors also want to thanks the Vice-Rector for Research at UNI for funding the publication of this work.

**Conflicts of Interest:** The authors declare no conflict of interest.

## Appendix A. Onset of the Absorption Edge

For the estimation of the optical gap of ZnO,  $E_g$ , we considered direct transitions, for which around  $E_g$  the absorption coefficient,  $\alpha$ , can be expressed as [46].

$$\alpha(h\nu) = A(h\nu - E_g)^{1/2}, \quad (\text{A1})$$

where  $h$  is Planck's constant,  $\nu$  is the frequency of the incident photon,  $A$  is a constant and  $E_g$  is the optical bandgap of thin film. Near the absorption edge the reflectance is much lower than the transmittance and nearly constant, then,  $\alpha$  can be obtained from:

$$\alpha = -\frac{\ln(T)}{d}. \quad (\text{A2})$$

## References

1. Nakata, K.; Tsuyoshi, O.; Taketoshi, M.; Fujishima, A. Photoenergy Conversion with TiO<sub>2</sub> Photocatalysis: New Materials and Recent Applications. *Electrochim. Acta* **2012**, *84*, 103–111. [[CrossRef](#)]
2. Ohtani, B. Photocatalysis A to Z—What We Know and What We Do Not Know in a Scientific Sense. *J. Photochem. Photobiol. C* **2010**, *11*, 157–178. [[CrossRef](#)]
3. Spasiano, D.; Marotta, R.; Malato, S.; Fernandez-Ibañez, P.; Di Somma, I. Solar Photocatalysis: Materials, Reactors, Some Commercial, and Pre-Industrialized Applications. A Comprehensive Approach. *Appl. Catal. B* **2015**, *170*, 90–123. [[CrossRef](#)]
4. Kansal, S.; Singh, M.; Sud, D. Studies on TiO<sub>2</sub>/ZnO photocatalysed degradation of lignin. *J. Hazard. Mater.* **2008**, *153*, 412–417. [[CrossRef](#)] [[PubMed](#)]
5. Li, Y.; Xie, W.; Hu, X.; Shen, G.; Zhou, X.; Xiang, Y.; Zhao, X.; Fang, P. Comparison of dye photodegradation and its coupling with light-to-electricity conversion over TiO<sub>2</sub>° and ZnO. *Langmuir* **2009**, *26*, 591–597. [[CrossRef](#)] [[PubMed](#)]
6. Coleman, V.A.; Jagadish, C. *Zinc Oxide Bulk, Thin Films and Nanostructures: Processing, Properties and Applications*; Elsevier: Amsterdam, The Netherlands, 2011; pp. 1–20.
7. Wang, Z.L. Nanostructures of zinc oxide. *Mater. Today* **2004**, *7*, 26–33. [[CrossRef](#)]
8. Ramos, P.G.; Morales, N.J.; Candal, R.J.; Hojamberdiev, M.; Rodriguez, J. Influence of zinc acetate content on the photoelectrochemical performance of zinc oxide nanostructures fabricated by electrospinning technique. *Nanomater. Nanotechnol.* **2016**, *6*. [[CrossRef](#)]
9. Fragalà, M.E.; Mauro, A.D.; Cristaldi, A.D.; Cantarella, M.; Impellizzeri, G.; Privitera, V. ZnO nanorods grown on ultrathin ZnO seed layers: Application in water treatment. *J. Photochem. Photobiol. A Chem.* **2017**, *332*, 497–504. [[CrossRef](#)]
10. Mauro, A.D.; Fragalà, M.E.; Privitera, V.; Impellizzeri, G. ZnO for application in photocatalysis: From thin films to nanostructures. *Mater. Sci. Semicond. Process.* **2017**, *69*, 44–51. [[CrossRef](#)]
11. Luo, L.; Lv, G.; Li, B.; Hu, X.; Jin, L.; Wang, J.; Tang, Y. Formation of aligned ZnO nanotube arrays by chemical etching and coupling with CdSe for photovoltaic application. *Thin Solid Films* **2010**, *518*, 5146–5152. [[CrossRef](#)]
12. Elias, J.; Tena-Zaera, R.; Lévy-Clément, C. Electrochemical deposition of ZnO nanowire arrays with tailored dimensions. *J. Electroanal. Chem.* **2008**, *621*, 171–177. [[CrossRef](#)]
13. Hari, P.; Baumer, M.; Tennyson, W.D.; Bumm, L.A. ZnO nanorod growth by chemical bath method. *J. Non-Cryst. Solids* **2008**, *354*, 2843–2848. [[CrossRef](#)]
14. Zhang, X.; Qin, J.; Xue, Y.; Yu, P.; Zhang, B.; Wang, L.; Liu, R. Effect of aspect ratio and surface defects on the photocatalytic activity of ZnO nanorods. *Sci. Rep.* **2014**, *4*, 4596. [[CrossRef](#)] [[PubMed](#)]
15. Wang, G.; Da, C.; Hao, Z.; Jin, Z.; Li, J. Tunable Photocurrent Spectrum in Well-Oriented Zinc Oxide Nanorod Arrays with Enhanced Photocatalytic Activity. *J. Phys. Chem. C* **2008**, *112*, 8850–8855. [[CrossRef](#)]
16. Wang, Z.; Liu, Y.; Huang, B.; Dai, Y.; Lou, Z.; Wang, G.; Zhang, X.; Qin, X. Progress on extending the light absorption spectra of photocatalysts. *Phys. Chem. Chem. Phys.* **2014**, *16*, 2758–2774. [[CrossRef](#)] [[PubMed](#)]
17. Samadi, M.; Zirak, M.; Naseri, A.; Khorashadizade, E.; Moshfegh, A.Z. Recent progress on doped ZnO nanostructures for visible-light photocatalysis. *Thin Solid Films* **2016**, *605*, 2–19. [[CrossRef](#)]

18. Chen, L.-C.; Tu, Y.-J.; Wang, Y.-S.; Kan, R.-S.; Huang, C.-M. Characterization and photoreactivity of N-, S-, and C-doped ZnO under UV and visible light illumination. *J. Photochem. Photobiol. A Chem.* **2008**, *199*, 170–178. [[CrossRef](#)]
19. Hatem, M.; Emilien, G.; Kevin, M.; Halima, A.; Ghouti, M.; Raphaël, S. ZnO rods/reduced graphene oxide composites prepared via a solvothermal reaction for efficient sunlight-driven photocatalysis. *Appl. Catal. B Environ.* **2016**, *185*, 11–21.
20. Salah, N.; Hameed, A.; Aslam, M.; Abdel-wahab, M.S.; Babkair, S.S.; Bahabri, F.S. Flow controlled fabrication of N doped ZnO thin films and estimation of their performance for sunlight photocatalytic decontamination of water. *Chem. Eng. J.* **2016**, *291*, 115–127. [[CrossRef](#)]
21. Qin, H.; Li, W.; Xia, Y.; He, T. Photocatalytic Activity of Heterostructures Based on ZnO and N-Doped ZnO. *ACS Appl. Mater. Interfaces* **2011**, *3*, 3152–3156. [[CrossRef](#)]
22. Kumari, R.; Sahai, A.; Goswami, N. Effect of nitrogen doping on structural and optical properties of ZnO nanoparticles. *Prog. Nat. Sci. Mater. Int.* **2015**, *25*, 300–309. [[CrossRef](#)]
23. Qiu, Y.; Fan, H.; Tan, G.; Yang, M.; Yang, X.; Yang, S. Effect of nitrogen doping on the photo-catalytic properties of nitrogen doped ZnO tetrapods. *Mater. Lett.* **2014**, *131*, 64–66. [[CrossRef](#)]
24. Park, J.Y.; Kim, S.M.; Lee, H.; Naik, B. Hot electron and surface plasmon-driven catalytic reaction in metal-semiconductor nanostructures. *Catal. Lett.* **2014**, *144*, 1996–2004. [[CrossRef](#)]
25. Ruiz Peralta, M.D.L.; Pal, U.; Zeferino, R.S. Photoluminescence (PL) quenching and enhanced photocatalytic activity of Au-decorated ZnO nanorods fabricated through microwave-assisted chemical synthesis. *ACS Appl. Mater. Interfaces* **2012**, *4*, 4807–4816. [[CrossRef](#)] [[PubMed](#)]
26. Xie, W.; Li, Y.; Sun, W.; Huang, J.; Xie, H.; Zhao, X. Surface modification of ZnO with Ag improves its photocatalytic efficiency and photostability. *J. Photochem. Photobiol. B* **2010**, *216*, 149–155. [[CrossRef](#)]
27. Dinesh, V.P.; Biji, P.; Ashok, A.; Dhara, S.K.; Kamruddin, M.; Tyagi, A.K.; Raj, B. Plasmon-mediated, highly enhanced photocatalytic degradation of industrial textile dyes using hybrid ZnO@Ag core-shell nanorods. *RSC Adv.* **2014**, *4*, 58930–58940. [[CrossRef](#)]
28. Chen, Y.; Tse, W.H.; Chen, L.; Zhang, J. Ag nanoparticles-decorated ZnO nanorod array on a mechanical flexible substrate with enhanced optical and antimicrobial properties. *Nanoscale Res. Lett.* **2015**, *10*, 106. [[CrossRef](#)]
29. Rodríguez, J.; Feuillet, G.; Donatini, F.; Onna, D.; Sanchez, L.; Candal, R.; Marchi, M.C.; Bilmes, S.A.; Chandezon, F. Influence of the spray pyrolysis seeding and growth parameters on the structure and optical properties of ZnO nanorod arrays. *Mater. Chem. Phys.* **2015**, *151*, 378–384. [[CrossRef](#)]
30. Quintana, M.; Ricra, E.; Rodríguez, J.; Estrada, W. Spray pyrolysis deposited zinc oxide films for photo-electrocatalytic degradation of methyl orange: Influence of the PH. *Catal. Today* **2002**, *76*, 141–148. [[CrossRef](#)]
31. Song, L.; Lim, S. Effect of Seed Layer on the Growth of ZnO Nanorods. *J. Phys. Chem. C* **2007**, *111*, 596–600. [[CrossRef](#)]
32. Ma, S.; Fang, G.; Li, C.; Sheng, S.; Fang, L.; Fu, Q.; Zhao, X.-Z. Controllable Synthesis of Vertically Aligned ZnO Nanorod Arrays in Aqueous Solution. *J. Nanosci. Nanotechnol.* **2006**, *6*, 2062–2066. [[CrossRef](#)] [[PubMed](#)]
33. Wu, W.-Y.; Yeh, C.-C.; Ting, J.-M. Effects of Seed Layer Characteristics on the Synthesis of ZnO Nanowires. *J. Am. Ceram. Soc.* **2009**, *92*, 2718–2723. [[CrossRef](#)]
34. Pokai, S.; Limnonthakul, P.; Horprathum, M.; Eiamchai, P.; Pattantsetakul, V.; Limwichean, S.; Nuntawong, N.; Porntheeraphat, S.; Chitichotpanya, C. Influence of seed layer thickness on well-aligned ZnO nanorods via hydrothermal method. *Mater. Proc.* **2017**, *4*, 6336–63341. [[CrossRef](#)]
35. Ghayour, H.; Rezaie, H.R.; Mirdamadi, S.; Nourbakhsh, A.A. The effect of seed layer thickness on alignment and morphology of ZnO nanorods. *Vacuum* **2011**, *86*, 101–105. [[CrossRef](#)]
36. Wang, M.; Ren, F.; Zhou, J.; Cai, G.; Cai, L.; Hu, Y.; Wang, D.; Liu, Y.; Guo, L.; Shen, S. N Doping to ZnO Nanorods for Photoelectrochemical Water Splitting under Visible Light: Engineered Impurity Distribution and Terraced Band Structure. *Sci. Rep.* **2015**, *5*. [[CrossRef](#)]
37. Cullity, B.D. *Elements of X-ray Diffraction*; Addison-Wesley: Reading, CA, USA, 1959.
38. Klingshirn, C.; Fallert, J.; Zhou, H.; Sartor, J.; Thiele, C.; Maier-Flaig, F.; Schneider, D.; Kalt, H. 65 years of ZnO research-old and very recent results. *Phys. Status Solidi. B* **2010**, *247*, 1424. [[CrossRef](#)]



39. Ahn, K.S.; Shet, S.; Deutsch, T.; Jiang, C.S.; Yan, Y.; Al-Jassim, M.; Turner, J. Enhancement of photoelectrochemical response by aligned nanorods in ZnO thin films. *J. Power Sources* **2008**, *176*, 387. [[CrossRef](#)]
40. Hirai, M.; Kumar, A. Effect of nitrogen doping on bonding state of ZnO thin films. *J. Vac. Sci. Technol. A* **2007**, *25*, 1534–1538. [[CrossRef](#)]
41. Shinde, S.S.; Bhosale, C.H.; Rajpure, K.Y. Photocatalytic degradation of toluene using sprayed N-doped ZnO thin films in aqueous suspension. *J. Photochem. Photobiol. B* **2012**, *113*, 70–77. [[CrossRef](#)]
42. Hatem, M.; Bilel, C.; Thomas, G.; Lavinia, B.; Kevin, M.; Ghouti, M.; Raphaël, S. Growth of ZnO Nanorods on Graphitic Carbon Nitride gCN Sheets for the Preparation of Photocatalysts with High Visible-Light Activity. *ChemCatChem* **2018**, *10*, 4973–4983.
43. Liu, H.; Hu, Y.; Zhang, Z.; Liu, X.; Jia, H.; Xu, B. Synthesis of spherical Ag/ZnO heterostructural composites with excellent photocatalytic activity under visible light and UV irradiation. *Appl. Surf. Sci.* **2015**, *355*, 644–652. [[CrossRef](#)]
44. Deng, Q.; Duan, X.; Ng, D.H.L.; Tang, H.; Yang, Y.; Kong, M.; Wu, Z.; Cai, W.; Wang, G. Ag Nanoparticle Decorated Nanoporous ZnO Microrods and Their Enhanced Photocatalytic Activities. *ACS Appl. Mater. Interfaces* **2012**, *4*, 6030–6037. [[CrossRef](#)] [[PubMed](#)]
45. Fageria, P.; Gangopadhyaya, S.; Pande, S. Synthesis of ZnO/Au and ZnO/Ag nanoparticles and their photocatalytic application using UV and visible light. *RSC Adv.* **2014**, *4*, 24962–24972. [[CrossRef](#)]
46. Erdogan, N.H.; Kara, K.; Ozdamar, H.; Kavak, H.; Esen, R.; Karaagac, H. Structural, optical and electrical properties of N-doped ZnO thin films prepared by thermal oxidation of pulsed filtered cathodic vacuum arc deposited Zn<sub>x</sub>Ny films. *J. Alloys Compd.* **2011**, *509*, 8922–8926. [[CrossRef](#)]
47. Ren, C.; Yang, B.; Wu, M.; Xu, J.; Fu, Z.; Lv, Y.; Guo, T.; Zhao, Y.; Zhu, C. Synthesis of Ag/ZnO nanorods array with enhanced photocatalytic performance. *J. Hazard. Mater.* **2010**, *182*, 123–129. [[CrossRef](#)]
48. Liu, J.; Li, J.; Wei, F.; Zhao, X.; Su, Y.; Han, X. Ag–ZnO Submicrometer Rod Arrays for High-Efficiency Photocatalytic Degradation of Congo Red and Disinfection. *ACS Sustain. Chem. Eng.* **2019**, *7*, 11258–11266. [[CrossRef](#)]
49. Kuriakose, S.; Choudhary, V.; Satpati, B.; Mohapatra, S. Enhanced photocatalytic activity of Ag–ZnO hybrid plasmonic nanostructures prepared by a facile wet chemical method. *Beilstein J. Nanotechnol.* **2014**, *5*, 639–650. [[CrossRef](#)]



© 2019 by the authors. Licensee MDPI, Basel, Switzerland. This article is an open access article distributed under the terms and conditions of the Creative Commons Attribution (CC BY) license (<http://creativecommons.org/licenses/by/4.0/>).